
Articulate your NeRF: Unsupervised articulated object modeling via conditional view synthesis

Jianning Deng Kartic Subr Hakan Bilen
University of Edinburgh
{jianning.deng, K.Subr, hbilen}@ed.ac.uk

Abstract

We propose a novel unsupervised method to learn pose and part-segmentation of articulated objects with rigid parts. Given two observations of an object in different articulation states, our method learns the geometry and appearance of object parts by using an implicit model from the first observation, distills the part segmentation and articulation from the second observation while rendering the latter observation. Additionally, to tackle the complexities in the joint optimization of part segmentation and articulation, we propose a voxel grid based initialization strategy and a decoupled optimization procedure. Compared to the prior unsupervised work, our model obtains significantly better performance, generalizes to objects with multiple parts while it can be efficiently from few views for the latter observation.

1 Introduction

Articulated objects, composed of multiple rigid parts connected by joints allowing rotational or translational motion, such as doors, cupboards and spectacles are ubiquitous in our daily lives. Automatically understanding the shape, structure and motion of these objects is crucial for numerous applications in robotic manipulation [12, 40] and character animation [1, 30]. Many works [10, 28, 32] focused on this problem use groundtruth 3D shape, articulation information, and/or part segmentation to learn articulated object models but acquiring accurate 3D observations and manual annotations is typically complex and too expensive for building real large-scale datasets.

In this paper, we introduce a novel unsupervised technique that learns part segmentation and articulation (*i.e.*, axis of movement, and translation/rotation of each movable part) from two sets of observations without requiring groundtruth shape, part segmentation or articulation. Each set contains images of an object from multiple viewpoints in different articulations. Our key idea is that articulation changes only the poses of the object parts, not their geometry or texture. Hence, once the geometry and appearance are learned, one can transform to another articulation state given the part locations and target articulation parameters.

Building on this idea, we frame the learning problem as a conditional novel articulation (and view) synthesis task (see Fig. 1(a)). Given a source observation with multiple views of an object in one articulation state, we first learn the object’s shape and appearance by using an implicit model [19] and freeze its weights. Next we pass the target observation – multi-view images of the same object in a different articulation state – to a tight bottleneck that distills part locations and articulations. We constrain our model to assign each 3D coordinate that is occupied by the object to a part and to apply a valid geometric transformation to the 3D coordinates of each part through ray geometry. The predictions of part segmentation and articulation, along with the target camera viewpoint, are passed to the implicit function and its differential renderer to reproduce the target observations (see Fig. 1(b)). Minimizing the photometric error between the rendered and target view provides supervision for learning part segmentation and articulation. However, joint optimization of these intertwined tasks are challenging and very sensitive to their initialization.

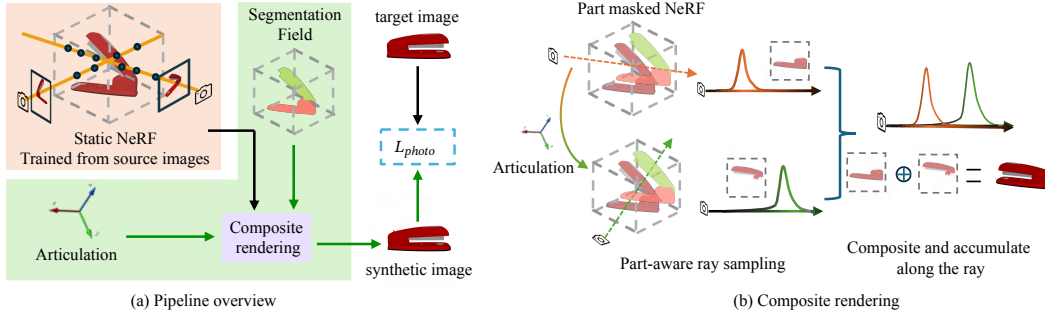


Figure 1: (a) Our method learns the geometry and appearance of an articulated object by first fitting a NeRF from (source) images of an object in a fixed articulation. Then, from another set of (target) images of the object in another articulation, we distill the relative articulation and part labels. Green lines show the gradient path during this distillation. (b) Using the part geometry and appearance from NeRF, we render the target images by compositing the parts after applying the predicted articulations to the segmented parts. The photometric error provides the required supervision for learning the parts and their articulation without groundtruth labels.

To address the optimization challenge, we propose an initialization strategy using an auxiliary voxel grid, which provides an initial estimate for moving parts by computing the errors in the foreground masks when rendering target views for the source articulation. Additionally, we introduce a decoupled optimization procedure that alternates between optimizing the part segmentation on the photometric error and the articulation parameters on the foreground prediction error.

The key advantage of our method, compared to other unsupervised articulation prediction methods [11, 15], is its stable performance across different object and articulation types, its ability to learn from few target views and to model multiple moving parts. Thanks to the stage-wise training, we achieve high-quality object geometry and appearance by using the well-optimized implicit models [2]. Since the part segmentation and articulation parameters form a small portion of the total weights, along with the initialization and decoupled optimization strategies, our method efficiently learns them from few target views, unlike the most relevant work [15] that jointly optimizes multiple part-specific implicit functions from scratch.

2 Related work

Analysis of articulated objects The analysis of articulated objects typically involves segmentation of movable parts, and estimating their attributes such as position and direction of joint axes, rotation angles, and translation distances. Prior works study articulated objects using 3D input such as meshes [29, 20], point clouds [42, 41, 35] or RGBD images [16, 6] that are error-prone and labor-intensive to collect in real-world scenarios. Recent works [10, 28, 32] that use RGB images to segment 3D planar object parts and estimate their articulation parameters simultaneously require ground-truth labels for segmentation and 3D articulation.

Articulated object modeling via novel view synthesis Neural implicit models [18, 24, 19] that are originally designed to model static objects in a 3D consistent way have been extended to articulated objects by multiple recent works [22, 34, 11, 14, 36, 15]. A-SDF [22] learns a disentangled latent space for shape and articulation to synthesize novel shapes and unseen articulated poses for a given object category. CARTO [7] extends A-SDF to multiple object categories and uses a stereo image pairs as input. Similarly, CLA-NeRF [34] learns to perform joint view synthesis, part segmentation, and articulated pose estimation for an object category from multiple views. NARF22 [14] learns a separate neural radiance fields (NeRF) for each part and composes to render the complete object. Unlike our method, both A-SDF and CARTO require 3D shape and articulation pose supervision, CLA-NeRF requires part segmentation labels and is limited to modeling only 1D revolutions for each joint, NARF22 relies on groundtruth part labels and articulation pose.

Most related to our work, DITTO [11] and PARIS [15] aim to estimate part segmentation and articulation pose without labels using from an observation pair of an object in two different articulations. DITTO uses a pair of point cloud as input, can only model shape, whereas both PARIS and our

method uses pairs of multi-view images, and to model both geometry and appearance. PARIS adopts the dynamic/static modelling of [39, 43], learns a separate NeRF for the dynamic and static parts. They are composited using the estimated relative articulation to render the observations with the different articulation. While our method is also based on the same analysis-by-synthesis principle to supervise the training, it differs from PARIS in several key ways. Our method involves only a single NeRF that is learned on multiple views of an object instance in a fixed articulation pose. Once the NeRF is learned, we freeze its parameters, and learn a segmentation head and articulation to selectively deform the rays while rendering views of different articulations. This means our model’s size remain nearly constant when the number of parts increases, which, combined with our two step optimization strategy, leads to more stable and data-efficient learning, yielding significantly better performance. Furthermore, we show that our model goes beyond modeling a single moving object part as in PARIS, and successfully learn multiple moving parts.

Deformable NeRF There exists several techniques [25, 27, 33, 26, 5] that model differences between subsequent video frames of a dynamic scene through a deformation field in 3D. While these techniques are general could be used in modeling articulated objects in principle, the deformation field does not provide explicit predictions for part segmentation and articulation. Prior methods that focus on modeling specific articulated and deformable objects such as human body [37, 31, 8, 9, 23] and four-legged animals [38] leverages specialized 3D priors [17] that are not applicable to arbitrary object categories.

3 Review: NeRF

Given a set of images \mathcal{I} of an object, a NeRF function [19] maps a tuple (\mathbf{x}, \mathbf{d}) , where $\mathbf{x} \in \mathbb{R}^3$ is a 3d position and $\mathbf{d} \in \mathbb{R}^2$ is a direction, to an RGB color \mathbf{c} , and a positive scalar volume density σ . The model outputs volume density σ at the location \mathbf{x} along with a latent feature vector z which is then concatenated with the viewing direction \mathbf{d} and fed into an MLP to estimate the view-dependent RGB color \mathbf{c} . With a slight abuse of notation, we also use σ and z as functions $\sigma(\mathbf{x})$ and $z(\mathbf{x})$ respectively and color as a function with $c(\mathbf{x}, \mathbf{d})$. That is, we use boldface to denote vectors.

NeRFs are trained by expressing the color at each pixel of images in the training subset. The color at a pixel C is estimated as C_N via the volume rendering equation as a sum of contributions from points along the ray through the pixel, say $r \in \mathcal{R}$. Points $\mathbf{x}_i, i = 1 \dots n$ are first sampled along the ray so that $\mathbf{x}_i = \mathbf{o} + t_i \mathbf{d}$ where \mathbf{o} is the origin of the ray (usually the point of projection of a camera view) and t_i is a scalar. Using these samples, the estimated color is given by

$$C_N(r) = \sum_{i=1}^n T_i^r (1 - \exp(-\sigma_i^r \delta_i^r)) \mathbf{c}_i^r \quad \text{where} \quad T_i^r = \sum_{j=1}^{i-1} \exp(-\sigma_j^r \delta_j^r) \quad (1)$$

where we use the shorthand notation \mathbf{c}_i^r and σ_i^r to denote $c(\mathbf{x}_i, \mathbf{d})$ and $\sigma(\mathbf{x}_i)$ respectively, and $\delta_i = t_{i+1} - t_i$ is the distance between samples. And the opacity value is calculated as: Similarly the opacity value for the pixel can be computed as $O_N(r) = \sum_{i=1}^n T_i^r (1 - \exp(-\sigma_i^r \delta_i^r))$. The parameters of c and σ are obtained by minimizing the photometric loss between predicted color $C_N(r)$ and the ground truth color $C(r)$ as

$$\mathcal{L}_{\text{photo}} = \sum_{r \in \mathcal{R}} \|C_N(r) - C(r)\|_2^2. \quad (2)$$

4 Method

Let \mathcal{I} and \mathcal{I}' be two observations of an object with k (known a priori) rigid parts in articulation poses \mathcal{P} and \mathcal{P}' respectively. Each observation contains multiple views of the object along with the foreground masks. We call \mathcal{I} the source observation and \mathcal{I}' the target observation. \mathcal{P} (resp. \mathcal{P}') is a pose tensor composed of $P_\ell \in SE(3)$, $\ell = 1 \dots k$ (resp. P'_ℓ) transformations as 4×4 matrices corresponding to the local pose of each of the k parts. Our primary goal is to estimate a pose-change tensor \mathcal{M} composed of $M_\ell \in SE(3)$, $\ell = 1 \dots k$ so that $P'_\ell = M_\ell P_\ell$. We solve this by starting with the construction of a NeRF from \mathcal{I} , as described in Sec. 3 along with the efficient coarse-to-fine volume sampling strategy in [2], followed by a novel modification to build awareness at the part-level. We use this modified parameterization to optimize an auxiliary voxel grid corresponding to the parts

via pose estimation and part segmentation pipelines. Once we have identified the parts and their relative transformations, we are able to re-render novel views corresponding to articulation pose \mathcal{P}' by transforming view rays suitably by M_ℓ^{-1} .

4.1 Part-aware rendering

Once a NeRF function, which we call ‘static NeRF’, is learned over \mathcal{I} , we freeze its parameters and append a segmentation head s to it towards obtaining part-level information. s is instantiated as 2-layer MLP, and maps the latent feature vector $z(\mathbf{x})$ to a probability distribution over the k object parts. We denote the probability of a 3D point \mathbf{x} to belong object part $\ell = 1 \cdots k$ as $s_\ell(z(\mathbf{x}))$.

If the segmentation class-probabilities s_ℓ and pose-change transformations M_ℓ are known, then the object in an unseen articulation pose can be synthesised by suitably transforming the statically trained NeRF without modifying its parameters and then compositing the individual part contributions. To model pose change in each part, we use a different ray, *virtual ray* associated with each part

$$r_\ell = M_\ell^{-1}r \quad (3)$$

and the final rendered color is:

$$C_P(r) = \sum_{i=1}^n \hat{T}_i^r \sum_{\ell=1}^k (1 - \exp(- (s_\ell^{r_\ell}(\mathbf{x}_i) \sigma^{r_\ell}(\mathbf{x}_i) \delta_j^{r_\ell}))) \mathbf{c}_i^{r_\ell} \quad (4)$$

where $\hat{T}_i^r = \sum_{j=1}^{i-1} \exp\left(-\sum_{\ell=1}^k (s_\ell^{r_\ell}(\mathbf{x}_j) \sigma^{r_\ell}(\mathbf{x}_j) \delta_j^{r_\ell})\right)$ is the transmittance sum. Compared to the original formulation in Eq. (1), it can be seen as the density replaced by a part-aware density which is the product of s and σ . Note that we made a similar modification to the efficient volume sampling strategy of [2] and refer to the Appendix A.1 for more details.

Since the groundtruth part segmentation and articulation are unknown, one could optimize the parameters of s and \mathcal{M} on the target observation such that the photometric error in between the part-aware rendered views and \mathcal{I}' . Note that $C_P(r)$ is function of \mathcal{M} (through r_ℓ in Eq. (3)) and s , they can be jointly optimized through backpropagation. However, jointly solving these two intertwined problems through rendering is challenging and highly sensitive to their initial values, as their solutions depend on each other. There, we introduce an alternating optimization strategy next.

4.2 Decoupled optimization of s and \mathcal{M}

To learn the part segmentation and pose-change, we first introduce an auxiliary voxel grid that assigns each 3D coordinate either to a background or a part. Once the voxel is initialized, our training iterates multiple times over a three-step procedure that includes optimization of \mathcal{M} , s , and refinement of the voxel grid entries.

Initialization of voxel grid Here our key idea is to find the pixel differences between the source and target observations by rendering a target view v' by using the static NeRF, and label the 3D locations of the different pixels as the movable parts to provide a good initialization for estimating the articulation (see Fig. 2). To this end, we first build a 3D voxel of the static NeRF by discretizing its 3D space into 128 bins along each dimension. To compute the voxel entries, we query the density value from the static NeRF at each voxel coordinate and binarize it into occupancy values with criteria $\exp(-\sigma(\mathbf{x})\delta) > 0.1$. Next, we use the static NeRF to render images for the viewpoints v' that are used to capture \mathcal{I}' . We compute difference in opacity value using O_N between these rendered images and the foreground masks of \mathcal{I}' , and binarize each value with 0.5 as threshold, and collect the ones that are not contained in the groundtruth foreground mask of the corresponding view in \mathcal{I}' . For those pixels, we further compute their depth by accumulating their density values along the corresponding ray, and use their estimated depth values to tag the occupied voxel entries either with static or dynamic parts. In the case of multiple moving parts, which is assumed to be known, we perform a clustering step [4] to identify $k - 1$ clusters corresponding to moving parts, as we assume that 1 part of the object is static without loss of generality. Finally, we gather the voxel coordinates that is assigned to part ℓ to form a matrix of 3D coordinates X_ℓ .

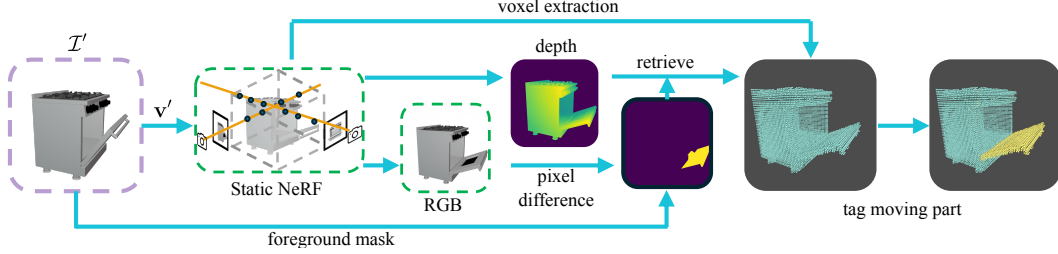


Figure 2: Voxel initialization: identify the voxels belonging to moved parts based on pixel opacity difference.

Step 1: Optimization of M_ℓ As depicted in Fig. 3, we project the 3D coordinates X_ℓ for part ℓ onto the image plane for each camera viewpoint v' included in \mathcal{T}' by using 3×4 dimensional intrinsic camera matrix K as $U_\ell = KM_\ell^{-1}v'X_\ell$, and denote the projected point matrix as U_ℓ . We concatenate the part-specific matrices to obtain U . As the groundtruth pixelwise part segmentation for part ℓ is unknown, we instead use the foreground masks for each view \mathcal{T}' that consists of all the part pixels, and stack the 2D coordinates to form the matrix F . Note that both U and F are matrices where each row corresponds to a 2D image coordinate where F has significantly more rows, as U is obtained from a coarse voxel grid. Then we minimize the 2D Chamfer distance between U and F :

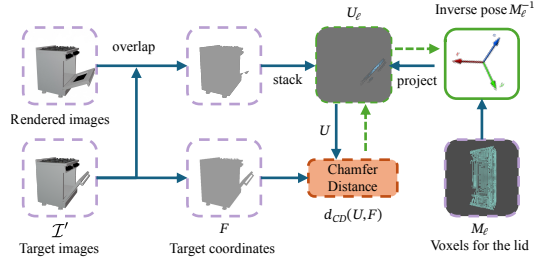


Figure 3: Illustration for optimization of M_ℓ . The green dotted line shows the gradient flow.

Then we minimize the 2D Chamfer distance between U and F :

$$\mathcal{M}^* = \arg \min_{\mathcal{M}} d_{CD}(U, F). \quad (5)$$

In practice, we only project X_ℓ for the moved parts, and stack them with 2D image coordinates of the foreground pixels in both the rendered image and the groundtruth image, as illustrated in Fig. 3.

Step 2: Optimization of s_ℓ Once we obtain the solution of the pose-change \mathcal{M}^* from Step 1, we plug it to the ray deformation in Eq. (3) and render each view in \mathcal{T}' in Eq. (4). Then we compute photometric loss between the rendered views and \mathcal{T}' , and minimize it with respect to the parameters of s only. In the case of multiple moving parts, we initialize the parameters in s using X_ℓ for supervision. Please refer to Appendix A.4 for more details.

Step 3: Voxel grid refinement The initial part segmentation estimates in the voxel grid are often sparse and noisy due to inaccurate density estimation in NeRF and misassignment of pixels around the foreground and part boundaries. To refine them, we build a 3D voxel again following steps in initialization stage, but we assign those 3D coordinates for different part ℓ based on the predicted label from segmentation head s . We denote the new 3D coordinates as X_ℓ^* . To maintain the consistency, we maintain and update voxels in X_ℓ^* only when the predicted part labels agree with the voxel labels within a 3D local neighborhood of X_ℓ . This neighborhood is defined as being within the distance of one grid cell at a resolution of 128. Then we update X_ℓ accordingly. Note that we only perform the refinement step, after approximately 2k iterations to ensure that the segmentation head produces confident results. Then we also increase the voxel resolution to 256 for each dimension.

5 Experiment

5.1 Dataset

We evaluate our method on the synthetic 3D PartNet-Mobility dataset [40, 21, 3]. While the dataset contains more than 2000 articulated objects from 46 different categories, we use a subset of the dataset with 6 shapes that was used in [15]. For a fair comparison, we downloaded the processed dataset from [15] which contains 2 sets of 100 views along with their foreground masks, each with a different articulation, and also groundtruth part segmentation labels, for each shape. In addition, we

Metric	Method	Revolut				Prismatic	
		laptop	oven	stapler	fridge	blade	storage
$e_d \downarrow$	PARIS	0.68 ± 0.40	1.04 ± 0.68	2.42 ± 0.91	0.81 ± 0.60	48.58 ± 25.43	0.34 ± 0.09
	Ours	0.33 ± 0.04	0.34 ± 0.03	0.33 ± 0.04	0.54 ± 0.08	1.54 ± 0.07	1.11 ± 0.14
$e_p \downarrow$ (10^{-2})	PARIS	0.18 ± 0.15	0.49 ± 0.53	55.54 ± 39.88	0.33 ± 0.14	-	-
	Ours	0.48 ± 0.06	1.29 ± 0.04	0.17 ± 0.05	0.44 ± 0.03	-	-
$e_g \downarrow$	PARIS	0.60 ± 0.32	0.68 ± 0.39	44.62 ± 6.17	0.87 ± 0.55	-	-
	Ours	0.25 ± 0.03	0.35 ± 0.06	0.290 ± 0.03	0.60 ± 0.05	-	-
$e_t \downarrow$	PARIS	-	-	-	-	1.13 ± 0.52	0.30 ± 0.01
	Ours	-	-	-	-	0.01 ± 0.01	0.02 ± 0.03

Table 1: **Part-level pose estimation results.** Our method outperforms PARIS in majority of object categories while having lower variation over multiple runs in the performance.

select 4 additional shapes, each with two moving parts, and apply the same data generation process to them. Additionally we collected images of a toy car with a handheld device, with camera viewpoint estimated from kiri engine application[13].

We train the static NeRF on 100 views from the first observation, train the part segmentation and articulation on 100 views from the second observation. We report the performance of our method for varying number of views from the second observation in Tab. 4.

Following [15], we report performance in different metrics for pose estimation, novel-view/articulation synthesis, and part segmentation. **Pose estimation:** To report articulation pose performance, we report results in i) direction error e_d that measures the angular discrepancy in degrees between the predicted and actual axis directions across all object categories, ii) position error e_p and geodesic distance e_d for only revolute objects to evaluate the error between the predicted and true axis positions and the error in the predicted rotation angles of parts in degrees, respectively, iii) translation error e_t to measure the disparity between the predicted and actual translation movements for prismatic objects. **Novel-view and -articulation synthesis:** We evaluate the quality of novel view synthesis generated by the models using the Peak Signal-to-Noise Ratio (PSNR) where higher values indicate better reconstruction fidelity. **Part segmentation:** We use mean Intersection over Union (mIoU) on the rendered semantic images to evaluate the accuracy of part segmentation, which is tightly related to the rendered image quality of objects in different articulation states. The ground truth segmentation is generated within the Sapien framework in [40]. Finally, due to the lack of groundtruth segmentation label and articulation in the real data, we only report PSNR and provide qualitative evaluation.

5.2 Results

Baseline We compare our approach with the state-of-the-art unsupervised technique, PARIS [15] which constructs separate NeRF models for each part of an articulated object and optimizes motion parameters in an end-to-end manner. However, it is limited to two-part objects with only one movable part. As the authors of PARIS do not report their results over multiple runs in their paper, we use their official public code with the default hyperparameters, train both their and our model over 5 random initializations and report the average performance and the standard deviation. We use 2 sets of 100 views for each object to train the models. More implementation details can be found in the supplementary material. We would like to note that the performance of PARIS in our experiments significantly differ from the original results despite all the care taken to reproduce them in the original way¹.

Part-level pose estimation For part-level pose estimation, we provide quantitative results in average performance over 5 runs and their standard deviations in Tab. 1, and a qualitative analysis in Fig. 6. The results indicate that our method consistently achieves lower errors across most evaluation metrics compared to PARIS, except the joint position error e_p where the differences are negligible, within the

¹Similar problems have been pointed out and the reproducibility of these results has been acknowledged as challenging by the authors in issue 1 and issue 2

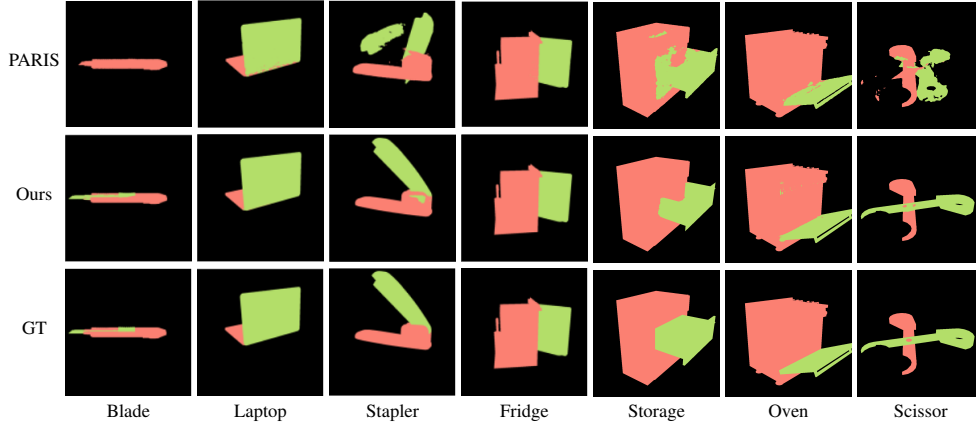


Figure 4: **Qualitative 2D part segmentation results.** Pixels in green denotes the movable parts. Our method demonstrates consistent performance across all tested objects while PARIS failed for Blade, Laptop and Scissor.

10^{-3} range. Notably, the performance of PARIS on the stapler and blade exhibits significantly higher errors. We observe that PARIS fails to converge to a good solution in all 5 runs for these objects. As shown in Fig. 6, PARIS fails to accurately segment the parts in the stapler and blade, which can also be easily identified in the novel articulation synthesis experiments in Fig. 6. Poor part reconstruction in PARIS results in inaccurate part-level pose estimations. Additionally, the lower standard deviation across all reconstructed objects for our method indicates its stable learning and ability to work for different object instances. We attribute the stability of our method to the decoupled optimization along with the stage-wise training, which contrasts with the joint optimization approach used by PARIS.

Segmentation and composite rendering Part segmentation and novel view synthesis in pose \mathcal{P}' are reported in Tab. 2, complemented by a qualitative analysis of part segmentation in Fig. 4. Our method outperforms PARIS across most evaluated objects in part segmentation and image synthesis quality, with the only exception being a minor difference in the PSNR for the laptop.

As our model builds on a static NeRF that achieves high quality novel view synthesis for one observation, the rendering quality is largely preserved after the second stage. We provide more detailed analysis in Appendix A.3. Additionally, benefiting from accurate pose estimation via a decoupled approach, our method achieves more robust and precise part segmentation, as depicted in Fig. 4. Here, our method consistently delivers accurate segmentation results for challenging objects such as the blade, stapler, and scissors, where PARIS struggles with accurate part reconstruction. In the other instances including the laptop, storage, and oven, our method achieves visibly better results.

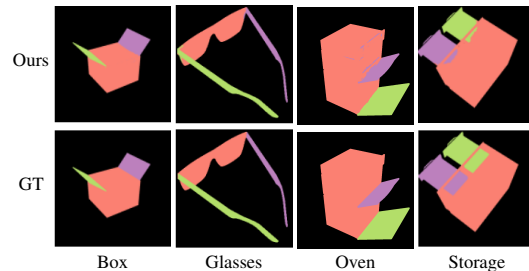


Figure 5: **Qualitative results for 2D multi-part segmentation.** The pink color denotes the static part, while other colors denote the moving parts.

Evaluation on objects with multiple movable parts A key advantage of our model is its ability to model objects with multiple moving parts. For such objects, we report pose estimation results in Tab. 3, qualitative for part segmentation in Fig. 5 and novel articulation synthesis in Fig. 6. As in the single part moving object experiments, our method consistently performs over the multi-part objects. Notably, we observed a marginally higher joint direction error for glasses, which we attribute to the thin structures such as temples and failure to segment them accurately which can be possibly improved by using higher resolution images.

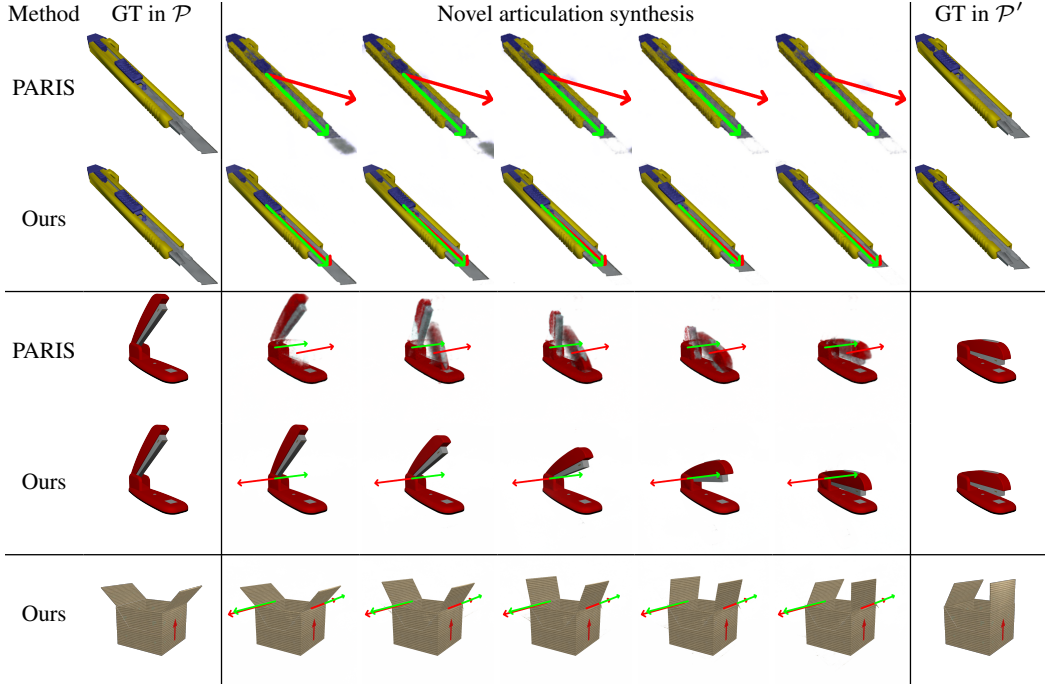


Figure 6: **Qualitative evaluation for novel articulation synthesis.** The ground truth axis is denoted in green and the predicted axis is denoted in red. Please refer to the supplementary for more visualizations.

5.3 Ablation studies

We assessed the effectiveness of the proposed decoupled pose estimation of M_ℓ (DP) and iterative refinement of X_ℓ (IR) on the ‘fridge’ object. When DP is disabled, the segmentation and articulation are simultaneously learned. In contrast, disabling IR maintains the initial X_ℓ for pose estimation. The results in Tab. 5, particularly the first row, demonstrate that joint optimization without DP inaccurately predicts the articulated pose, treating the entire object as static. While enabling DP improves the performance, as shown in the second row, the performance is still poor due to the noisy initial values compared to our full model.

Additionally, we evaluated the impact of the number of views in the target observation for training. We train our model on the randomly subsampled views for multiple runs and averaged their performance (see Tab. 4). Results show a significant drop in pose estimation and rendering quality with 4 images or less. Notably, even with only 8 images, our approach surpasses the performance of PARIS trained with 100 images (indicated with subscript P in Tab. 4). This result clearly shows that our method is more robust against fewer viewpoints from the target viewpoints and allows efficiently learning ‘articulate’ a pretrained NeRF from few target views only.

Metric	Method	Revolut				Prismatic	
		laptop	oven	stapler	fridge	blade	storage
mIoU \uparrow	PARIS	0.98	0.99	0.16	0.98	0.76	0.94
	Ours	0.99	0.99	0.98	0.99	0.94	0.96
PSNR \uparrow	PARIS	30.31	31.48	24.36	32.74	31.87	30.63
	Ours	29.27	32.08	34.31	35.10	36.47	34.51

Table 2: **Articulation synthesis and part segmentation results.** Average performance over 5 runs (best results in boldface).

Metric	Revolut			Prismatic
	oven	glasses	box	storage
$e_d \downarrow$	1.02	2.35	0.56	1.82
$e_p \downarrow$	0.16	0.47	0.27	-
$e_g \downarrow$	1.03	1.01	0.65	-
$e_t \downarrow (10)$	-	-	-	0.11
PSNR \uparrow	32.98	29.22	28.61	28.25
mIoU \uparrow	0.97	0.98	0.99	0.94

Table 3: **Objects with multiple parts.** Errors using multiple metrics for pose estimation (averaged over all joints).

Metric	Num. of images						
	2	4	8	16	32	100	100 \mathcal{P}
$e_d \downarrow$	46.05	8.89	0.59	0.58	0.50	0.54	0.81
$e_g \downarrow$	44.74	20.79	0.70	0.60	0.56	0.49	0.87
PSNR \uparrow	22.65	29.95	34.00	34.28	34.88	35.10	32.74

Table 4: Ablation studies with different number of target images.

Init.		Metric		
DP	IR	e_d	e_g	PSNR
-	-	2.57	26.95	18.09
\checkmark	-	2.38	14.96	25.16
\checkmark	\checkmark	0.54	0.49	35.10

Table 5: Ablation study over different initialization strategies.

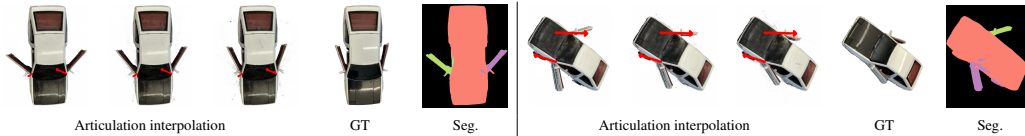


Figure 7: Results on real world examples, the red line indicates the estimated joint axis direction. Green and purple color denotes the moving car door, while pink denotes the body of the toy car. Please refer to Fig. 12 for more qualitative evaluation.

5.4 Real-world example

The qualitative evaluation can be found in Fig. 7. The pose \mathcal{P} for training the static NeRF is with two doors wide open, and the reconstruction results from NeRF is shown in the first row in Fig. 7. Qualitative comparison for ground truth images in pose \mathcal{P}' is presented in second and third row of Fig. 7. The average PSNR we obtain from the static NeRF is , and the PSNR for 28.19, while the PSNR for pose \mathcal{P}' is 24.32. More detail results for segmentaion and articulation interpolation are also presented in Fig. 7.

5.5 Limitations

Our method has few limitations too. As we use rendering to supervise our segmentation and pose, our method may fail to segment very thin parts when the rendering error is small. When the object parts are nearly symmetry, our method may fail to find the correct articulation and choose another articulation that produces similar rendering. We provide examples of such failure cases in Appendix A.3. Additionally, it also inherits the limitations of the implicit models that are built on such as failure to model transparent objects, and inaccurate 3D modeling when the viewpoint information is noisy. Finally, our method is limited to articulated objects with rigid parts and cannot be used to model soft tissue deformations.

6 Conclusion

In this study, we tackled the challenges of self-supervised part segmentation, articulated pose estimation, and novel articulation rendering for objects with multiple movable parts. Our approach is the first known attempt to model multipart articulated objects using only multi-view images acquired from two arbitrary articulation states of the same object. We evaluated our method with both synthetic and real-world datasets. The results suggest that our method competently estimates part segmentation and articulation pose parameters, and effectively renders images of unseen articulations, showing promising improvements over existing state-of-the-art techniques. Further, our real-world data experiments underscore the method’s robust generalization capabilities. At last, the code and the data used in this project will be released upon acceptance. However, the reliance on geometric information from moving parts for articulation pose estimation poses challenges in modeling highly symmetrical objects. Future work could improve our method by incorporating both appearance and geometric data into the pose estimation process, potentially enhancing accuracy and applicability.

Broader Impacts The proposed technique could be potentially used to understand articulated objects for their robotic manipulation in future. The authors are not aware of any potential harm that may arise when the technology is used

References

- [1] Norman Badler, Brian Barsky, and David Zeltzer. *Making Them Move: Mechanics, Control & Animation of Articulated Figures*. Routledge, 1990.
- [2] Jonathan T Barron, Ben Mildenhall, Dor Verbin, Pratul P Srinivasan, and Peter Hedman. Mipnerf 360: Unbounded anti-aliased neural radiance fields. In *Proceedings of the IEEE/CVF Conference on Computer Vision and Pattern Recognition*, pages 5470–5479, 2022.
- [3] Angel X Chang, Thomas Funkhouser, Leonidas Guibas, Pat Hanrahan, Qixing Huang, Zimo Li, Silvio Savarese, Manolis Savva, Shuran Song, Hao Su, et al. Shapenet: An information-rich 3d model repository. *arXiv preprint arXiv:1512.03012*, 2015.
- [4] Martin Ester, Hans-Peter Kriegel, Jörg Sander, and Xiaowei Xu. Density-based spatial clustering of applications with noise. In *Int. Conf. knowledge discovery and data mining*, volume 240, 1996.
- [5] Jiemin Fang, Taoran Yi, Xinggang Wang, Lingxi Xie, Xiaopeng Zhang, Wenyu Liu, Matthias Nießner, and Qi Tian. Fast dynamic radiance fields with time-aware neural voxels. In *SIGGRAPH Asia 2022 Conference Papers*, pages 1–9, 2022.
- [6] Haoran Geng, Helin Xu, Chengyang Zhao, Chao Xu, Li Yi, Siyuan Huang, and He Wang. Gapartnet: Cross-category domain-generalizable object perception and manipulation via generalizable and actionable parts. In *Proceedings of the IEEE/CVF Conference on Computer Vision and Pattern Recognition*, pages 7081–7091, 2023.
- [7] Nick Heppert, Muhammad Zubair Irshad, Sergey Zakharov, Katherine Liu, Rares Andrei Ambrus, Jeannette Bohg, Abhinav Valada, and Thomas Kollar. Carto: Category and joint agnostic reconstruction of articulated objects. In *Proceedings of the IEEE/CVF Conference on Computer Vision and Pattern Recognition*, pages 21201–21210, 2023.
- [8] Zeng Huang, Yuanlu Xu, Christoph Lassner, Hao Li, and Tony Tung. Arch: Animatable reconstruction of clothed humans. In *Proceedings of the IEEE/CVF Conference on Computer Vision and Pattern Recognition*, pages 3093–3102, 2020.
- [9] Mustafa Işık, Martin Rünz, Markos Georgopoulos, Taras Khakhulin, Jonathan Starck, Lourdes Agapito, and Matthias Nießner. Humanrf: High-fidelity neural radiance fields for humans in motion. *ACM Transactions on Graphics (TOG)*, 42(4):1–12, 2023.
- [10] Hanxiao Jiang, Yongsan Mao, Manolis Savva, and Angel X Chang. Opd: Single-view 3d openable part detection. In *European Conference on Computer Vision*, pages 410–426. Springer, 2022.
- [11] Zhenyu Jiang, Cheng-Chun Hsu, and Yuke Zhu. Ditto: Building digital twins of articulated objects from interaction. In *Proceedings of the IEEE/CVF Conference on Computer Vision and Pattern Recognition*, pages 5616–5626, 2022.
- [12] Dov Katz and Oliver Brock. Manipulating articulated objects with interactive perception. In *2008 IEEE International Conference on Robotics and Automation*, pages 272–277. IEEE, 2008.
- [13] KIRI Innovation. Kiri engine.
- [14] Stanley Lewis, Jana Pavlasek, and Odest Chadwicke Jenkins. Narf22: Neural articulated radiance fields for configuration-aware rendering. In *2022 IEEE/RSJ International Conference on Intelligent Robots and Systems (IROS)*, pages 770–777. IEEE, 2022.
- [15] Jiayi Liu, Ali Mahdavi-Amiri, and Manolis Savva. Paris: Part-level reconstruction and motion analysis for articulated objects. In *Proceedings of the IEEE/CVF International Conference on Computer Vision*, pages 352–363, 2023.
- [16] Liu Liu, Han Xue, Wenqiang Xu, Haoyuan Fu, and Cewu Lu. Toward real-world category-level articulation pose estimation. *IEEE Transactions on Image Processing*, 31:1072–1083, 2022.
- [17] Matthew Loper, Naureen Mahmood, Javier Romero, Gerard Pons-Moll, and Michael J. Black. SMPL: A skinned multi-person linear model. *ACM Trans. Graphics (Proc. SIGGRAPH Asia)*, 34(6):248:1–248:16, October 2015.
- [18] Lars Mescheder, Michael Oechsle, Michael Niemeyer, Sebastian Nowozin, and Andreas Geiger. Occupancy networks: Learning 3d reconstruction in function space. In *Proceedings of the IEEE/CVF conference on computer vision and pattern recognition*, pages 4460–4470, 2019.

- [19] Ben Mildenhall, Pratul P Srinivasan, Matthew Tancik, Jonathan T Barron, Ravi Ramamoorthi, and Ren Ng. Nerf: Representing scenes as neural radiance fields for view synthesis. *Communications of the ACM*, 65(1):99–106, 2021.
- [20] Niloy J Mitra, Yong-Liang Yang, Dong-Ming Yan, Wilmot Li, Maneesh Agrawala, et al. Illustrating how mechanical assemblies work. *ACM Transactions on Graphics-TOG*, 29(4):58, 2010.
- [21] Kaichun Mo, Shilin Zhu, Angel X. Chang, Li Yi, Subarna Tripathi, Leonidas J. Guibas, and Hao Su. PartNet: A large-scale benchmark for fine-grained and hierarchical part-level 3D object understanding. In *The IEEE Conference on Computer Vision and Pattern Recognition (CVPR)*, June 2019.
- [22] Jiteng Mu, Weichao Qiu, Adam Kortylewski, Alan Yuille, Nuno Vasconcelos, and Xiaolong Wang. A-sdf: Learning disentangled signed distance functions for articulated shape representation. In *Proceedings of the IEEE/CVF International Conference on Computer Vision*, pages 13001–13011, 2021.
- [23] Atsuhiko Noguchi, Xiao Sun, Stephen Lin, and Tatsuya Harada. Neural articulated radiance field. In *Proceedings of the IEEE/CVF International Conference on Computer Vision*, pages 5762–5772, 2021.
- [24] Jeong Joon Park, Peter Florence, Julian Straub, Richard Newcombe, and Steven Lovegrove. DeepSDF: Learning continuous signed distance functions for shape representation. In *Proceedings of the IEEE/CVF conference on computer vision and pattern recognition*, pages 165–174, 2019.
- [25] Keunhong Park, Utkarsh Sinha, Jonathan T Barron, Sofien Bouaziz, Dan B Goldman, Steven M Seitz, and Ricardo Martin-Brualla. Nerfies: Deformable neural radiance fields. In *Proceedings of the IEEE/CVF International Conference on Computer Vision*, pages 5865–5874, 2021.
- [26] Keunhong Park, Utkarsh Sinha, Peter Hedman, Jonathan T Barron, Sofien Bouaziz, Dan B Goldman, Ricardo Martin-Brualla, and Steven M Seitz. Hypernerf: A higher-dimensional representation for topologically varying neural radiance fields. *arXiv preprint arXiv:2106.13228*, 2021.
- [27] Albert Pumarola, Enric Corona, Gerard Pons-Moll, and Francesc Moreno-Noguer. D-nerf: Neural radiance fields for dynamic scenes. In *Proceedings of the IEEE/CVF Conference on Computer Vision and Pattern Recognition*, pages 10318–10327, 2021.
- [28] Shengyi Qian, Linyi Jin, Chris Rockwell, Siyi Chen, and David F Fouhey. Understanding 3d object articulation in internet videos. In *Proceedings of the IEEE/CVF Conference on Computer Vision and Pattern Recognition*, pages 1599–1609, 2022.
- [29] Andrei Sharf, Hui Huang, Cheng Liang, Jiawei Zhang, Baoquan Chen, and Minglun Gong. Mobility-trees for indoor scenes manipulation. In *Computer Graphics Forum*, volume 33, pages 2–14. Wiley Online Library, 2014.
- [30] Aliaksandr Siarohin, Oliver J Woodford, Jian Ren, Menglei Chai, and Sergey Tulyakov. Motion representations for articulated animation. In *Proceedings of the IEEE/CVF Conference on Computer Vision and Pattern Recognition*, pages 13653–13662, 2021.
- [31] Shih-Yang Su, Frank Yu, Michael Zollhöfer, and Helge Rhodin. A-nerf: Articulated neural radiance fields for learning human shape, appearance, and pose. *Advances in Neural Information Processing Systems*, 34:12278–12291, 2021.
- [32] Xiaohao Sun, Hanxiao Jiang, Manolis Savva, and Angel Xuan Chang. Opdmulti: Openable part detection for multiple objects. *arXiv preprint arXiv:2303.14087*, 2023.
- [33] Edgar Tretschk, Ayush Tewari, Vladislav Golyanik, Michael Zollhöfer, Christoph Lassner, and Christian Theobalt. Non-rigid neural radiance fields: Reconstruction and novel view synthesis of a dynamic scene from monocular video. In *Proceedings of the IEEE/CVF International Conference on Computer Vision*, pages 12959–12970, 2021.
- [34] Wei-Cheng Tseng, Hung-Ju Liao, Lin Yen-Chen, and Min Sun. Cla-nerf: Category-level articulated neural radiance field. In *2022 International Conference on Robotics and Automation (ICRA)*, pages 8454–8460. IEEE, 2022.

- [35] Xiaogang Wang, Bin Zhou, Yahao Shi, Xiaowu Chen, Qinpeng Zhao, and Kai Xu. Shape2motion: Joint analysis of motion parts and attributes from 3d shapes. In *Proceedings of the IEEE/CVF Conference on Computer Vision and Pattern Recognition*, pages 8876–8884, 2019.
- [36] Fangyin Wei, Rohan Chabra, Lingni Ma, Christoph Lassner, Michael Zollhöfer, Szymon Rusinkiewicz, Chris Sweeney, Richard Newcombe, and Mira Slavcheva. Self-supervised neural articulated shape and appearance models. In *Proceedings of the IEEE/CVF Conference on Computer Vision and Pattern Recognition*, pages 15816–15826, 2022.
- [37] Chung-Yi Weng, Brian Curless, Pratul P Srinivasan, Jonathan T Barron, and Ira Kemelmacher-Shlizerman. Humannerf: Free-viewpoint rendering of moving people from monocular video. In *Proceedings of the IEEE/CVF conference on computer vision and pattern Recognition*, pages 16210–16220, 2022.
- [38] Shangzhe Wu, Ruining Li, Tomas Jakab, Christian Rupprecht, and Andrea Vedaldi. Magicpony: Learning articulated 3d animals in the wild. In *Proceedings of the IEEE/CVF Conference on Computer Vision and Pattern Recognition*, pages 8792–8802, 2023.
- [39] Tianhao Wu, Fangcheng Zhong, Andrea Tagliasacchi, Forrester Cole, and Cengiz Oztireli. D²nerf: Self-supervised decoupling of dynamic and static objects from a monocular video. *Advances in neural information processing systems*, 35:32653–32666, 2022.
- [40] Fanbo Xiang, Yuzhe Qin, Kaichun Mo, Yikuan Xia, Hao Zhu, Fangchen Liu, Minghua Liu, Hanxiao Jiang, Yifu Yuan, He Wang, Li Yi, Angel X. Chang, Leonidas J. Guibas, and Hao Su. SAPIEN: A simulated part-based interactive environment. In *The IEEE Conference on Computer Vision and Pattern Recognition (CVPR)*, June 2020.
- [41] Li Yi, Haibin Huang, Difan Liu, Evangelos Kalogerakis, Hao Su, and Leonidas Guibas. Deep part induction from articulated object pairs. *arXiv preprint arXiv:1809.07417*, 2018.
- [42] Qing Yuan, Guiqing Li, Kai Xu, Xudong Chen, and Hui Huang. Space-time co-segmentation of articulated point cloud sequences. In *Computer Graphics Forum*, volume 35, pages 419–429. Wiley Online Library, 2016.
- [43] Wentao Yuan, Zhaoyang Lv, Tanner Schmidt, and Steven Lovegrove. Star: Self-supervised tracking and reconstruction of rigid objects in motion with neural rendering. In *Proceedings of the IEEE/CVF Conference on Computer Vision and Pattern Recognition*, pages 13144–13152, 2021.

Metric	Method	Revolut				Prismatic	
		laptop	oven	stapler	fridge	blade	storage
$e_d \downarrow$	PARIS [†]	0.03	0.03	0.07	0.00	0.00	<u>0.37</u>
	PARIS	<u>0.18</u>	0.48	1.30	<u>0.22</u>	<u>0.27</u>	0.24
	Ours	0.26	<u>0.28</u>	<u>0.27</u>	0.42	1.41	0.86
$e_p \downarrow$ (10^{-2})	PARIS [†]	0.01	0.03	0.06	0.02	-	-
	PARIS	<u>0.08</u>	<u>0.04</u>	2.12	<u>0.17</u>	-	-
	Ours	0.39	1.24	<u>0.13</u>	0.41	-	-
$e_g \downarrow$	PARIS [†]	0.03	0.00	0.00	0.00	-	-
	PARIS	0.24	<u>0.25</u>	37.86	<u>0.37</u>	-	-
	Ours	<u>0.22</u>	0.31	<u>0.24</u>	0.55	-	-
$e_t \downarrow$ (10^{-1})	PARIS [†]	-	-	-	-	0.06	0.00
	PARIS	-	-	-	-	5.84	2.93
	Ours	-	-	-	-	<u>0.12</u>	<u>0.05</u>

Table 6: Comparison with PARIS in 5-time best setting. PARIS[†] denotes performance reported in the original paper. Best results are shown in **bold**, second best are shown with underline.

A Appendix / supplemental material

Optionally include supplemental material (complete proofs, additional experiments and plots) in appendix. All such materials **SHOULD be included in the main submission**.

A.1 Part-aware proposal network

To achieve part-aware composite rendering for articulated objects, we also need to modify the proposal network for correct sampling along the ray $r \in \mathcal{R}'$. In the composite rendering, the proposal network is now required to produce the similar distribution of the weights for samples along the ray. Thus, following the similar design in the part-aware NeRF, we append an extra segmentation field to the proposal network. Now the valid density for each samples becomes segmentation-mask density as $s_{\ell}^{r_e}(x_j)\sigma^{r_e}$. The transmittance are then calculated using Eq. (4) without the color term, which will be later used for online distillation. Please refer to the original paper [2] for more details about the online distillation. During the training of part-aware NeRF, the original parameters in the proposal network will be frozen and only updates the segmentation field.

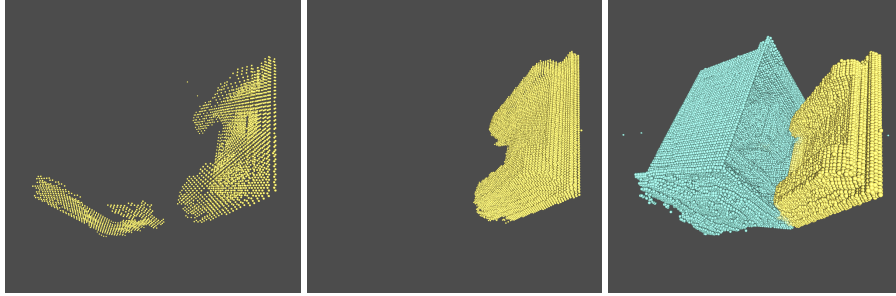
A.2 Comparison with PARIS

Here we also provide the 5-time best comparison between ours and PARIS. Besides, the reported performance for PARIS is also provided in this subsection. From Tab. 6, we can see that the original reported performance from PARIS are exceptionally better compared to the reproduced ones, even though with the same data and the same configurations. If we only focus on the 5-time best comparison between reproduced PARIS and ours, we can see that we achieve comparable performance. Another thing we can notice is that for prismatic objects, while PARIS has much better estimations on joint axis direction. However, our method later show much better estimation for estimating the moved distance for the dynamic parts. While one thing to notice is that PARIS failed to reconstruct the stapler for all 5 runs in our experiment.

A.3 Limitations

Details about the limitations and failure cases of our methods.

In our decoupled optimization strategy, the articulated pose estimation relies exclusively on the geometric information from the moving parts. As a result, our method faces challenges with highly



(a) Visualization of dynamic voxel update. From left to right: initialized X_ℓ , updated X_ℓ , final X_ℓ



(b) Failure cases for foldchair, from left to right: groundtruth RGB, rendered RGB, part segmentation.



(c) Artifacts for thin parts, the left one is the groundtruth, the right rendering result.

symmetrical components. For example, in the case of a folding chair Appendix A.3, although the segmentation accurately identifies the chair’s seat, the pose estimation mistakenly flips the seat by 180 degrees, resulting in the seat being oriented with the bottom upwards as shown in Fig. 8(b). Additionally, our method may encounter difficulties when the articulation motion is minimal, which can lead to insufficient pixel differentiation in images across different articulation poses for initial model estimation. In such cases, both the pose estimator and the iterative updates of X_ℓ may underperform or even fail. We also notice that the proposal network have difficulties handling very thin parts in the novel articulation synthesis. As we can see in Appendix A.3, some artifacts appeared at the edge of the frame and the temples for the glasses as in Fig. 8(c), which should be ideally masked out without any opacity and color for those pixels.

Furthermore, the reliance on a pre-trained static NeRF limits the upper boundary of our method’s performance in rendering novel articulations. Addressing these limitations could significantly enhance the robustness and applicability of our strategy in handling complex articulated objects. For further analysis of this, please refer to .

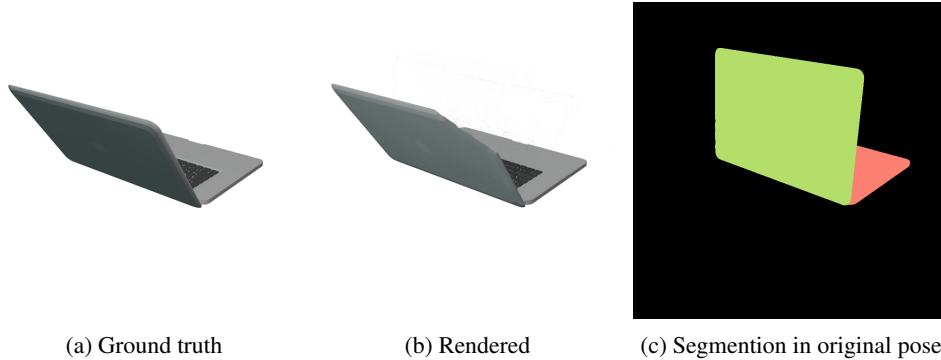


Figure 9: We can see in the Fig. 9(b) that the corner of the laptop screen is missing in the novel articulation rendering. While it looks perfect when we check the segmentation in the original pose. Thus, we suspect it is the proposal network that failed to estimate the density distribution for the screen from certain viewpoints.

A.4 Training setting

As detailed in Sec. 4.2, we perform optimization on M_ℓ for 4000 iterations and on s_ℓ for 2000 iterations for all evaluated objects. Checkpoints are saved following Step 3. We conduct this process through 5 cycles for objects with a single moving part and 6 cycles for objects with multiple moving parts. Checkpoints with best PSNR during validation will be used for test.

During the first step of M_ℓ optimization, we begin with a learning rate of 0.01, which linearly decays by 0.5 every 500 iterations. We accumulate gradients from 8 viewpoints to simulate a batch size of 8, initializing M_ℓ identically in the first cycle and using the previously estimated M_ℓ for subsequent cycles.

In the second step of s_ℓ optimization using the Adam optimizer, the initial learning rate is set at 0.01 and linearly decays by a factor of 0.01 every 100 iterations. For multiple moving parts, initialization involves training the segmentation head s using pre-assigned labels on X_ℓ , and querying predictions for $x \in X_\ell$. Cross-entropy loss optimized over 1000 iterations with a learning rate of $1e^{-3}$ shapes the learnable parameters in s .

Our experiments, requiring around 16 GB of VRAM, complete in approximately 30 minutes on a single RTX 4090 GPU for a single object. As for the training of static NeRF, it takes about 10 minutes with less than 10 GB of VRAM. The estimated total GPU time for this project would be about 2 GPU months.

A.5 Ablations

A.5.1 Performance cost for novel articulation synthesis

We also provide an ablation study to investigate the performance drops for conditional novel articulation synthesis compared to the pre-trained static model. As shown in Tab. 7, the performance drop is subject to different category of objects ranging from smallest 13.3% for the fridge and blade to 31.4% laptop. We suspect the significant drops for laptop is caused by the deteriorate performance of the proposal network on the thin laptop screen. Visualizations can be found in Fig. 9. The results indicate that our method can benefit from the high quality of appearance reconstruction from the pre-trained static NeRF.

A.6 Visualization

Here we show more visualization for qualitative evaluations. Besides, additional animated images for the real-world toy car is also provided in the supplementary materials.

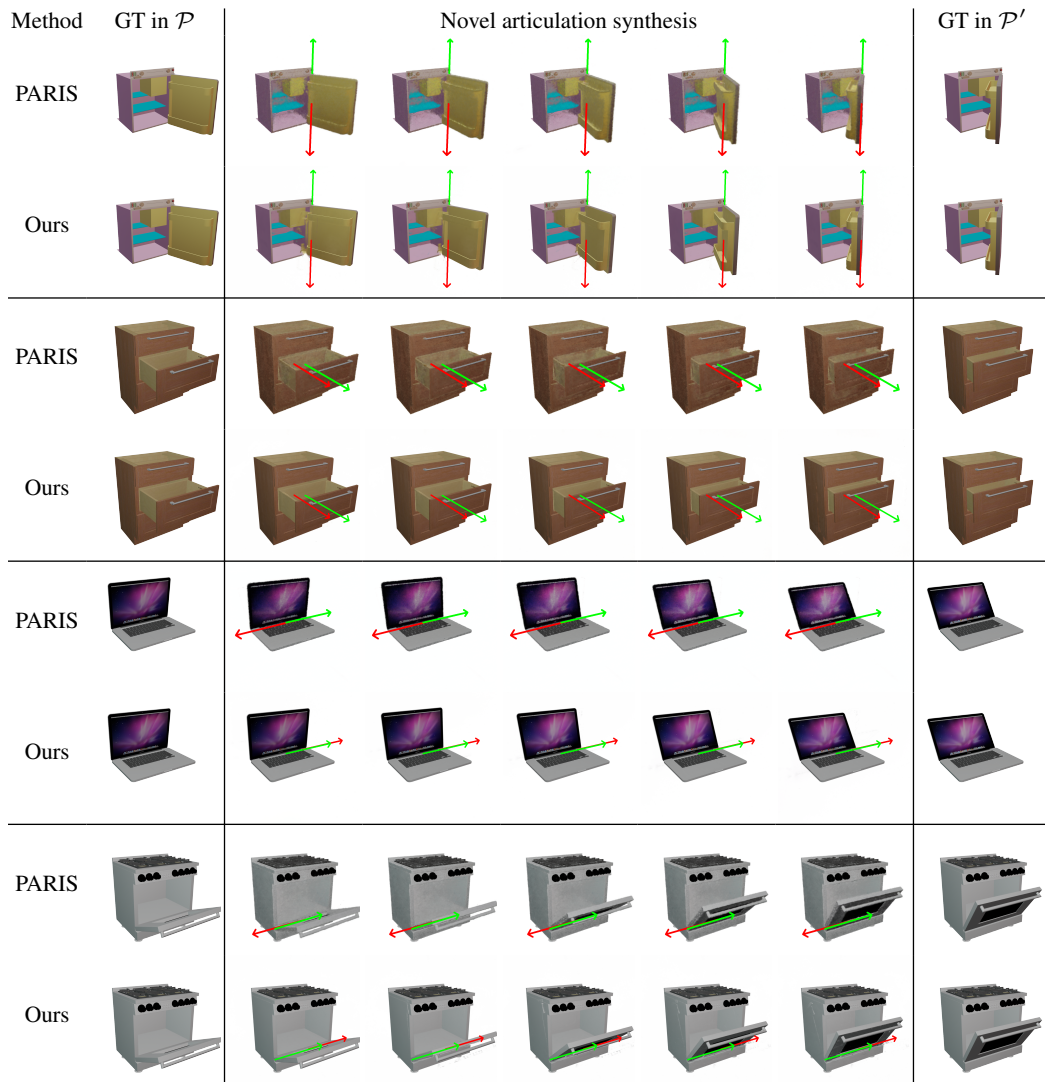


Figure 10: Articulation interpolation for single moving part objects.

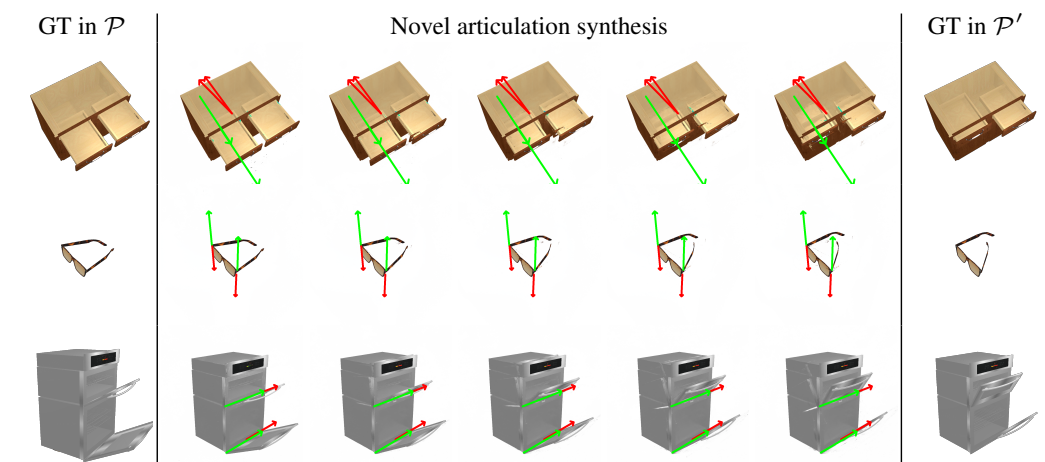
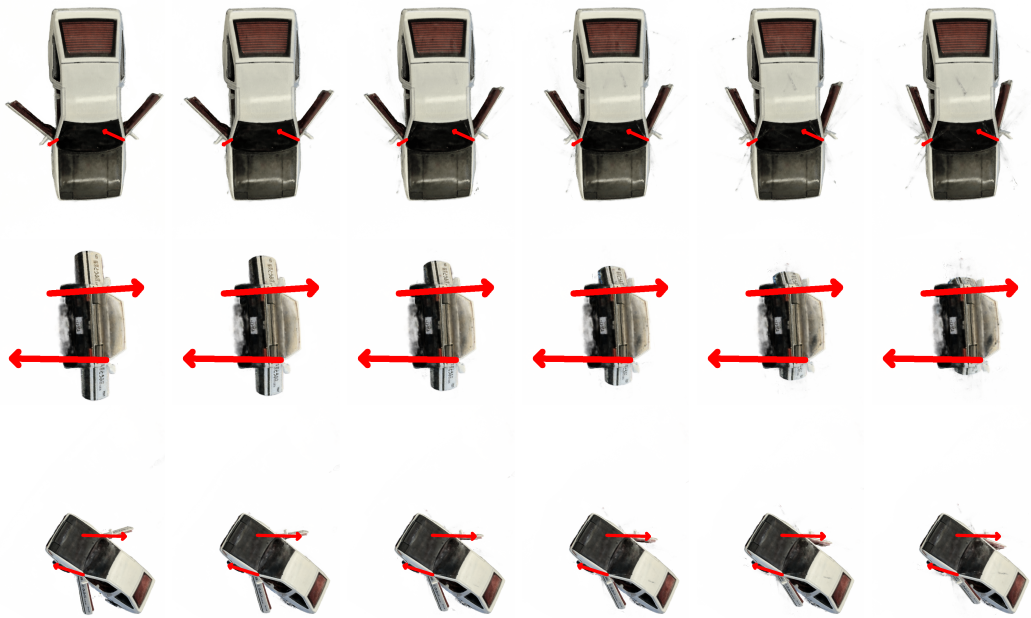


Figure 11: Articulation interpolation for multiple moving part objects.

Method	Object									
	laptop	oven	stapler	fridge	blade	storage	oven*	glasses*	box*	storage*
Static	42.70	39.69	42.39	40.50	42.7	40.33	39.03	37.93	36.56	35.23
Art.	29.27	32.08	34.31	35.1	36.47	34.51	32.98	29.22	28.61	28.25
Δ	-31.4%	-19.2%	-19.1%	-13.30%	-13.3%	-14.4%	-15.5%	-22.8%	-21.8%	-19.8%

Table 7: Comparison of rendering quality between objects in their original pose \mathcal{P} and articulated pose \mathcal{P}' . 'Static' refers to the rendering performance of the object in its original pose \mathcal{P} , whereas 'Art.' indicates the rendering quality of the object in articulated pose \mathcal{P}' using our method with the static NeRF. Objects marked with * represent those with multiple movable parts.

Novel articulation synthesis



Segmentation

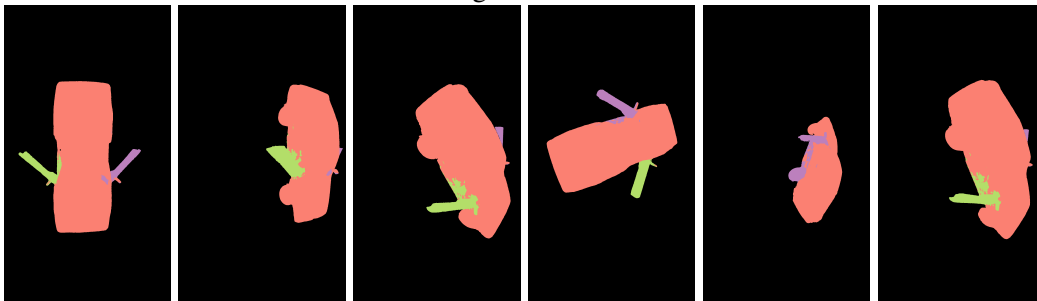


Figure 12: More Qualitative evaluation on real-world object.